



Wind wave growth in the viscous regime

Jiarong Wu ¹ and Luc Deike ^{1,2,*}

¹*Department of Mechanical and Aerospace Engineering, Princeton University, Princeton, New Jersey 08544, USA*

²*High Meadows Environmental Institute, Princeton University, Princeton, New Jersey 08544, USA*



(Received 3 March 2021; accepted 24 August 2021; published 8 September 2021)

We investigate the growth of short gravity-capillary waves due to wind forcing, solving the two-phase Navier-Stokes equations. The numerical method features a momentum conserving scheme, interface reconstruction using volume of fluid, and adaptive mesh refinement. A 2D laminar wind profile is used to force short gravity-capillary waves in the viscous regime, and the growth of the wave amplitude and subsurface drift layer are analyzed. The threshold for wave growth is found to depend on a balance between the growth rate and viscous dissipation rate, while the wave growth for all data can be described as a scaling depending on wind stress and a viscous correction accounting for the growth threshold. Together with the wave growth, the subsurface drift layer develops and can be described in terms of a similarity solution. The nonlinear stage of wave growth is discussed for increasing wavelength, and we recover steep capillary waves, parasitic capillary waves, and spilling breakers depending on the ratio of gravity to surface tension forces.

DOI: [10.1103/PhysRevFluids.6.094801](https://doi.org/10.1103/PhysRevFluids.6.094801)

I. INTRODUCTION

Wind-wave interaction happens when wind blows across the water surface, causing the wave amplitude to grow under the wind forcing. The physics of this common but complex phenomenon has been studied for over half a century in numerous theoretical, experimental, and numerical works (see the reviews from [1,2]). The seminal theoretical contributions of Miles [3] and Phillips [4] serve as baseline of our current understanding. The growth rate of wind waves has been theoretically studied by solving the Orr-Sommerfeld equations with investigations of the role of the wind profile and viscosity [5,6]. Separately, many experimental measurements both at sea and in the laboratory, supported by the theoretical analysis of Miles', suggest a growth rate that scales with the inverse wave age u_*/c [7], with c the wave phase speed and u_* the wind friction velocity,

$$\bar{\beta} = 2\pi\alpha \frac{\rho_a}{\rho_w} \left(\frac{u_*}{c} \right)^2, \quad (1)$$

where $\bar{\beta} = \beta T$ is the nondimensional growth rate, with β the growth rate and T the wave period, related to the wavelength by the wave dispersion relation; ρ_a/ρ_w is the air-water density ratio; and α is an $O(10)$ constant adjusted to the data. However, scatter in data remains, and there are controversies over how applicable this formula is in different regimes [8], in particular for short waves where viscous effects might be important, and for steep waves where air-flow separation might occur. This is related to the many difficulties in determining the momentum and energy transfer from wind to waves under given conditions [9]. The small density ratio ρ_a/ρ_w makes growth

*ldeike@princeton.edu

rate small and precise measurement difficult; and wind wave interaction happens across a wide range of wave scales, from capillary-gravity waves [$O(\text{mm})$ to $O(\text{cm})$], to young gravity waves [$O(1\text{ m})$ – $O(10\text{ m})$] to swells [$O(100\text{ m})$], and the dynamics and interplay with the surrounding turbulent flow vary across the different scales. The wind field above the waves is a turbulent boundary layer, characterized by high Reynolds number turbulence, which is difficult to formulate analytically; besides, the wave effect on turbulent boundary layer is still an open question [10,11]; the coupling with the underlying currents is important in certain regimes [1]; and, last but not least, there are very limited spatially and temporally well-resolved experimental data [9,12] due to understandable difficulties of making measurement close to the water surface.

These challenges have motivated numerical investigations over the years. However, numerical simulations are also restricted by the aforementioned difficulties. Large eddy simulation (LES) [13–15] is a preferred method when studying large-scale wind wave interaction [$O(1\text{ m})$ – $O(100\text{ m})$] since it resolves only large scales and dynamically important eddies in turbulence and is therefore computationally more effective. The challenge lies in including the small-scale effect within subgrid scale modeling, in this case the representation of waves and their interaction with turbulence below the grid resolution. This is usually done with a roughness length parametrization on a purely empirical basis (see, e.g., [14,15]), although there are some recent efforts made towards dynamic modeling of the roughness (see, e.g., [16]). In other words, it implicitly assumes accurate knowledge of the momentum flux into small-scale waves. Direct numerical simulation (DNS), on the other hand, has the advantage of resolving all small-scale transfer processes without models, but is limited in the range of scales and Reynolds numbers it can achieve. Another major difficulty facing both LES and DNS methods is the treatment of the coupling between two phases. Often times this coupling is one-sided. With works focused on the waves' effects on the turbulent boundary layer [11], the waves are usually reduced to a boundary with prescribed shape and motion; with works focusing on wave growth, on the other hand, the wind is often reduced to a pressure forcing term [17,18]. There are still very few simulations achieving a two-way coupled simulation. Lin *et al.* [19] performed DNS on two sets of equations for both phases, with linearized kinetic and dynamic boundary conditions at the interface. Yang and Shen [20] described in detail the numerical procedure for both DNS coupled with a potential wave solver and DNS coupled with DNS, and several working cases are given. In each configuration, complex boundary conditions and grid mapping have to be implemented.

We approach this long-standing problem with a different numerical method, leveraging progress in adaptive mesh refinement algorithms for two-phase flows with the open source solver Basilisk [21–24], including a geometric volume of fluid (VoF) interface reconstruction, a momentum conserving scheme, and adaptive mesh refinement. Solving for a two-phase shear flow with a deformable free surface is a challenging numerical problem, especially when large density and viscosity ratios are involved. Numerical methods implemented within Basilisk are tailored to such problems, and these methods have previously been applied to the modeling of a two-phase mixing layer [25] demonstrating very good agreement with the solution of the Orr-Sommerfield eigenvalue problem. The VoF interface tracking method is particularly valuable because it eliminates the need of any prescribed boundary conditions at the interface and is not limited to linear wave regimes. Hence, these methods have recently been used to study deep and shallow water breaking waves [23,26,27]. These features differentiate our numerical approach from previous work and offer a promising avenue for fully coupled wind-wave simulations.

As a first step towards a fully coupled 3D simulation with a turbulent boundary layer, in this paper we present a laminar 2D configuration, with a linear wind shear profile, representing a constant shear stress, forcing a single gravity-capillary wave. We investigate the small-scale dynamics of waves of $O(1\text{ mm})$ to $O(1\text{ cm})$ where a large part of the wind stress is supported by viscous shear stress and viscous damping is important, which might help understand the role of viscosity in the initial stages of wind-wave growth with the development of a viscous shear layer underneath the wave. In addition, it serves as a test of the ability of our numerical methods to resolve momentum and energy transfer from a wind shear layer to a wave field.

Viscous effects in wind wave growth have received limited attention [28]. When large-scale wind wave interaction and high Reynolds numbers are considered, they usually come as a correction term representing viscous wave dissipation, $-4\nu_w k^2/\omega$ to the total wave growth [7,9,29]. However, the viscous effects remain crucial to wave onset criteria and lower Reynolds number wave growth, as discussed experimentally and theoretically [28,30] with implications for the wind speed threshold for wrinkles and regular waves, and for the subsequent spatial growth rate. Solving the full Navier-Stokes equation with viscosity also means that we can investigate the water drift layer under surface shear stress, which is known to be relevant for wind-forced waves [31] and has been experimentally observed during wind wave onset [32,33]. The interplay between the wave growth and the drift layer has been studied in the context of wave-current interaction (e.g., [34]) with an established current profile. Our simulation setup reflects a more realistic concurrent development of wave and subsurface drift, relevant to the existing theories of wave-current interaction.

The paper is organized as follows. In Sec. II we outline the governing equation and the numerical method, and introduce the important nondimensional parameters. In Sec. III we introduce a heuristic decomposition of the flow into a wave field and a drift layer. This allows separate studies of wave growth and drift development. Finally in Sec. IV we discuss the subsequent nonlinear stages of wind-wave growth, and for increasing Bond number (ratio of gravity to surface tension forces), we recover nonlinear capillary waves (low Bond number), parasitic capillary waves formed at the front of steep waves (intermediate Bond number), and spilling breakers (high Bond number). We present a qualitative discussion of these wave regimes, in close agreement with the existing numerical and experimental literature.

As a note of caution, we acknowledge that a laminar linear profile is not the wind profile above large-scale waves at the ocean-atmosphere interface, which is typically characterized by a logarithmic profile. However, this study is relevant for small-scale viscous gravity-capillary waves, where the upper boundary layer profile might not affect the wave growth, and for waves in microfluidic systems [35]. This setup also serves as a validation of the numerical methods for wind-wave studies, while the challenging generalization to three-dimensional simulations of wind-wave forced by a turbulent boundary layer will be the goal of future work.

II. SIMULATION SETUP

A. Governing equations and numerical method

We use the two-phase Navier-Stokes solver Basilisk [21,22], with adaptive mesh refinement. The two-phase incompressible Navier-Stokes equations are solved with a momentum conserving scheme, and the interface between two immiscible fluids is captured by a geometric volume of fluid (VoF) method. As such, we do not solve two separate sets of equations for each phase and connect them with certain boundary conditions at the interface. We solve the variable density and viscosity Navier-Stokes equations:

$$\begin{aligned} \partial_t \rho + \nabla \cdot (\rho \mathbf{u}) &= 0, \\ \rho[\partial_t \mathbf{u} + (\mathbf{u} \cdot \nabla) \mathbf{u}] &= -\nabla p + \nabla \cdot (2\mu \mathbf{D}) + \sigma \kappa \delta_S(\mathbf{x} - \mathbf{x}_{\mathcal{F}}) \mathbf{n}, \end{aligned} \quad (2)$$

where $D_{ij} \equiv (\partial_i u_j + \partial_j u_i)/2$ is the strain rate tensor. Surface tension is represented by $\sigma \kappa \delta_S \mathbf{n}$ as an interfacial force, $\delta_S(\mathbf{x} - \mathbf{x}_{\mathcal{F}})$ is the Dirac function ($\mathbf{x}_{\mathcal{F}}$ is the surface location defined by \mathcal{F}), and σ , κ , \mathbf{n} are surface tension, curvature and the normal vector of the interface, respectively. The interface is tracked with a volume fraction field $\mathcal{F}(\mathbf{x}, t)$. The geometric VoF method is sharp in the sense that the interface is located within one cell and \mathcal{F} goes from 0 to 1 within one cell. The density ρ and viscosity μ are arithmetic averages of water and air densities ρ_w and ρ_a , and viscosities μ_w and μ_a , i.e., $\rho = \mathcal{F} \rho_w + (1 - \mathcal{F}) \rho_a$, $\mu = \mathcal{F} \mu_w + (1 - \mathcal{F}) \mu_a$. The momentum is advected consistently with the field \mathcal{F} so that the total momentum is conserved, which is critical in the wind wave problem. These choices of numerical methods make the fewest assumptions of the nature of the wind wave interaction and allow full coupling between the two phases. We use adaptive mesh refinement to

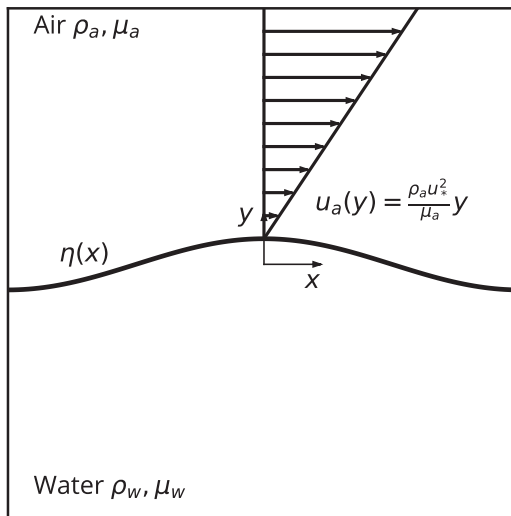


FIG. 1. Sketch of the simulation setup: a linear small amplitude (exaggerated in the sketch) wave $\eta(x)$ is initialized in the water, with phase speed c , forced by a constant slope linear shear layer in the air, $u_a(y)$. The strength of the wind forcing is characterized by the ratio between the air friction velocity u_* and the phase speed c . The computational domain is a one wave length by one wave length square, and the origin is set in the center, at mean water level.

gain a high resolution at the interface while keeping the total computational cost manageable. We consider a maximum level of refinement of 11 in most of the cases presented here, equivalent to a fixed grid of size $2^{11} = 2048$ per wavelength. Tests for grid convergence with level of refinement up to 12 have been performed, and all results presented in the paper have been verified for grid convergence as summarized in Appendix A.

B. Initial and boundary conditions, nondimensional variables

The initial conditions are sketched in Fig. 1. The wave interface $\eta(\mathbf{x}, 0)$ and orbital velocity are initialized with a linear wave solution and a small slope $a_0 k$:

$$\eta(\mathbf{x}, 0) = a_0 \cos(kx), \quad (3)$$

$$u(\mathbf{x}, 0) = a_0 \omega \frac{\cosh[k(y+h)]}{\sinh(kh)} \cos(kx), \quad (4)$$

$$v(\mathbf{x}, 0) = a_0 \omega \frac{\sinh[k(y+h)]}{\sinh(kh)} \sin(kx), \quad (5)$$

where

$$\omega = \sqrt{\tilde{g} k \tanh(kh)} \quad (6)$$

is the dispersion relation for finite depth gravity-capillary wave [36], and $\tilde{g} = g + \sigma k^2 / \rho_w$ is the modified gravitational acceleration to account for surface tension. The wave number $k = 2\pi / L_0$ is such that there is one wave in the computational domain $L_0 \times L_0$, and it propagates in the x direction with periodic boundary conditions left and right. The bottom wall is free-slip, and we have verified that the water depth $h = L_0 / 2$ is a good enough approximation of the deep water wave condition. The wave slope has little impact on the initial wave growth in the present configuration (which has also been verified by simulations) as long as it is in the small amplitude regime, i.e., the slope

TABLE I. Wave and wind parameters used in the simulation: the physical wavelength and corresponding matching Bond and Reynolds numbers. Bo and Re are computed with gravitational acceleration $g = 9.8 \text{ m/s}^2$, surface tension $\sigma = 0.074 \text{ N/m}$ and water density $\rho_w = 1 \times 10^3 \text{ kg/m}^3$. The inverse wave age varies from 0.4 to 1 to determine the wave growth threshold as a function of the Reynolds number. We also conducted cases with higher Bond number 25 and 200 to discuss the role of Bond number at fixed Re, and discuss the nonlinear stages and associated dynamical features when the wave reaches a high slope. These cases can be interpreted as corresponding to water waves of wavelength 0.086 m and 0.244 m while being more viscous than water waves of the same wavelength.

Wavelength [cm]	Bo	Re	u_*/c
0.9	0.27	2587	0.7, 0.8, 0.9, 1.0
1.3	0.53	3389	0.6, 0.7, 0.8, 0.9, 1.0
2.1	1.47	5513	0.4, 0.5, 0.6, 0.7, 0.8, 0.9, 1.0
3.1	3.31	9105	0.4, 0.5, 0.6, 0.7
8.6	25	5513	0.4, 0.6, 1.0
24.4	200	5513	0.4, 0.6, 1.0

remains below 0.1. Therefore, all the following discussions on the initial growth rates are based on cases with an initial slope $a_0k = 0.05$, and growth rates are computed before ak reaches 0.1.

We consider a linear velocity profile to represent the wind close to the interface, as shown in Fig. 1. The slope of the profile is specified by $\rho_a u_*^2 / \mu_a$ (slightly altered by the presence of the waves), where u_* is the air friction velocity widely used in wind wave literature to quantify the strength of the wind forcing. This represents a constant shear stress condition with $\tau = \rho_a u_*^2$ (we have verified that the change of the profile slope, i.e., τ during the simulated wave growing time is negligible). The top wall boundary conditions are constant tangential velocity based on the given average slope and zero normal velocity. As explained in the introduction, this linear profile is inspired by our focus on small-scale waves and allows us to consider a 2D laminar air flow that is steady away from the surface.

The relevant variables in this simplified 2D laminar wind-wave problem are $\rho_a, \rho_w, \mu_a, \mu_w, a_0, k, g, \sigma$, and u_* . Dimensional analysis gives that the problem is defined by six nondimensional numbers. We consider the water-air density and viscosity ratios ρ_w/ρ_a and μ_w/μ_a , the initial wave slope a_0k , the inverse wave age u_*/c (quantifying the strength of wind forcing), the Reynolds number Re (characterizing the viscosity versus inertial effect), and the Bond number Bo (characterizing the relative importance of surface tension versus gravity). The actual water and air viscosity and density ratios are used across all simulations, i.e., $\rho_w/\rho_a = 850/1$, and $\mu_w/\mu_a = 8.9 \times 10^{-4}/17.4 \times 10^{-6}$ and a_0k is fixed to be 0.05. We are left with three controlling nondimensional numbers u_*/c , Re, and Bo:

$$u_*/c, \text{ Re} = \frac{\rho_w c \lambda}{\mu_w}, \text{ Bo} = \frac{(\rho_w - \rho_a)g}{\sigma k^2}, \quad (7)$$

where c is the linear phase speed for gravity-capillary wave and λ is the wavelength,

$$c = \omega/k = \sqrt{g \tanh(kh)/k}, \quad \lambda = 2\pi/k. \quad (8)$$

For the majority of the cases, we match the choice of Bo and Re such that they correspond to real water waves of certain wavelengths (see Table I) and consider four sets of simulations, while sweeping the wind forcing u_*/c from 0.4 to 1, which corresponds to relevant values for the growth of short waves considering the very early wave growth stage when the wave phase speed is small. This wavelength range is close to the onset wavelength for wind waves reported in [28]. We are limited in the highest Reynolds number because of the numerical instability that large shear induces in the linear wind profile, when the laminar flow becomes unstable with the development of 2D shear instabilities, which is not desirable in the current setting.

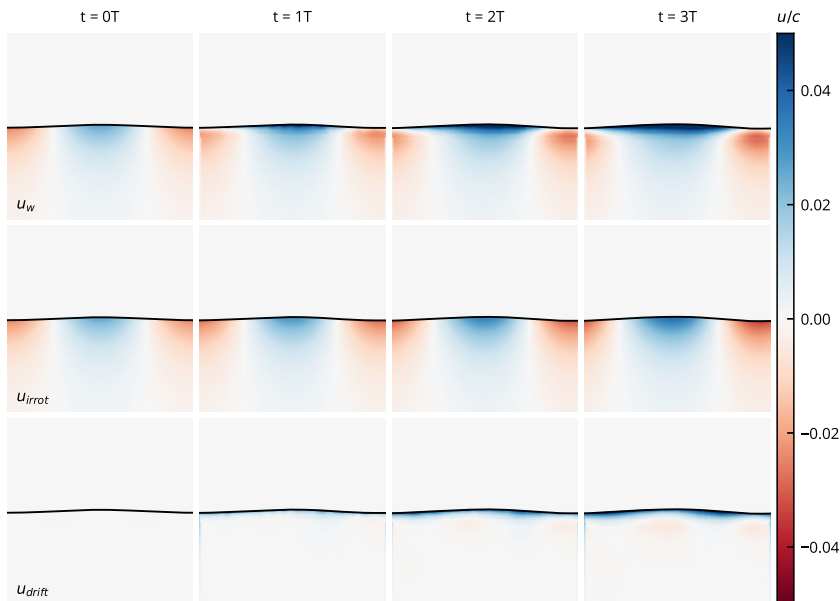


FIG. 2. Snapshots showing an example of the wave and drift growth. The first row shows the wave interface (in black) and the horizontal water velocity field in color. Decompositions between irrotational (horizontal) wave velocity u_{irrot} and drift velocity u_{drift} are shown in the second and third rows. u_{irrot} is computed from surface elevation $\eta(x, t)$. The increase of wave amplitude, drift velocity, and thickening of the drift layer during several wave periods can be seen clearly. The initial stages of growth are similar for all cases; shown here is $\text{Re} = 5513$, $\text{Bo} = 1.47$, and $u_* / c = 1$.

We also performed a sequence of cases at fixed Reynolds number, $\text{Re} = 5513$, and increasing Bond number, $\text{Bo} = 25, 200, 1000$ (thus not matching the Re of air-water waves), for wind forcing $u_* / c = 0.4, 0.6$, and 1 . This set of simulations will be used to discuss the Bond number effect on the initial growth rate as well as the later development of the wave into nonlinear dynamics.

III. CONCURRENT WAVE AND DRIFT GROWTH

A. Wave and drift growth under wind forcing

Figure 2 shows a typical wind wave growing case, for $\text{Re} = 5513$, $\text{Bo} = 1.47$, and $u_* / c = 1$ (corresponding to a wavelength of 2.1 cm). The first row shows the wave amplitude together with the velocity field in the propagating direction, $u(x, y)$. As the wind blows, the wave amplitude increases and a thin shear layer underwater develops, which we call surface drift. We observe concurrent growth of the wave and the drift layer: the wave amplitude becomes higher while the drift layer thickens and the surface drift velocity increases. We initially focus on this growth regime, with small amplitude and developing shear layer; thus, the simulations are run for four wave periods or until the slope ak has doubled to reach 0.1. We also ran some cases to study later stages and nonlinear features, and they will be discussed in Sec. IV. The surface drift layer has been experimentally discussed in [32,33], in the context of wave growth inception, and considered as DNS initialization in [19], but is often ignored in numerical studies, especially when a potential flow solver is used [16].

To discuss the growth of the surface drift and the wave amplitude separately, within these initial stages at low amplitude, we decompose the velocity field into two parts. The irrotational part $\mathbf{u}_{\text{irrot}}$ (second row) is computed in a similar way to Eqs. (4) and (5),

with higher order correction terms, assuming that the wave shape resembles a Stokes wave [37]:

$$\eta(\mathbf{x}, t) = a(t) \cos \phi(\mathbf{x}, t) + \epsilon \eta_1 + \epsilon^2 \eta_2, \quad (9)$$

$$u_{\text{irrot}}(\mathbf{x}, t) = a(t) \omega \frac{\cosh[k(y+h)]}{\sinh(kh)} \cos \phi(\mathbf{x}, t) + \epsilon u_1 + \epsilon^2 u_2, \quad (10)$$

$$v_{\text{irrot}}(\mathbf{x}, t) = a(t) \omega \frac{\sinh[k(y+h)]}{\sinh(kh)} \sin \phi(\mathbf{x}, t) + \epsilon v_1 + \epsilon^2 v_2; \quad (11)$$

$\epsilon = a(t)k$ is the instantaneous steepness and the small parameter of the nonlinear expansion. $\eta_1, \eta_2, u_1, u_2, v_1, v_2$ are first- and second-order correction terms; see [26] for the full expression. There is also a nonlinear correction to angular frequency $\omega = \sqrt{gk \tanh(kh)} \{1 + \epsilon^2 [(9/8)(\chi^2 - 1)^2 + \chi^2]\}$, where $\chi = 1/\tanh(kh)$, but in practice the finite depth effect is negligible in our setup. In principle, the wave shape should deviate from that of a Stokes wave due to the presence of the drift layer and capillarity, but this effect is neglected in this analysis of the initial stage. Note that because of the low amplitude, the obtained drift would be similar if the linear approximation had been used.

This decomposition requires the simulation output of the wave phase $\phi(\mathbf{x}, t)$ and a time dependent amplitude $a(t)$. We extract the phase $\phi(\mathbf{x}, t)$ from the surface elevation $\eta(x, t)$ by performing a Hilbert transform (as discussed when analyzing experimental data in [10]). The time-varying amplitude is then computed from integrating $\eta(x, t)$:

$$a(t)^2 = 2 \int_0^{L_0} \eta(x, t)^2 dx / L_0. \quad (12)$$

We subtract $\mathbf{u}_{\text{irrot}}$ from the total velocity field \mathbf{u}_w (first row in Fig. 2) to get the rotational part \mathbf{u}_{rot} (third row),

$$\mathbf{u}_{\text{rot}} = \mathbf{u}_w - \mathbf{u}_{\text{irrot}}. \quad (13)$$

We assume that the rotational part \mathbf{u}_{rot} is approximately the drift velocity $\mathbf{u}_{\text{drift}}$. Free traveling waves (without wind forcing) in a viscous fluid also have a thin layer of vorticity near the surface that is of alternating signs, but we have verified that this contribution is at least an order of magnitude smaller than the vorticity of the drift (see Appendix B for details). Therefore we ignore the wave vorticity part, and take \mathbf{u}_{rot} as an approximation of $\mathbf{u}_{\text{drift}}$, and use only the notation $\mathbf{u}_{\text{drift}}$ for the following discussion. Of course, this approximation is not as accurate in the nonlinear stages. Figure 2 shows in the second row the irrotational part of the velocity field obtained through this decomposition, which grows in intensity together with the wave amplitude, while the third row shows the drift velocity with a thin layer developing and intensifying as time advances.

In the following sections we discuss the growth of the wave and drift respectively. It is found that the respective wave energy budget and drift growth pattern are similar for all Re, Bo, and inverse wave age u_* / c , but the relative growth of wave and drift can change across Re and Bo under the same u_* / c .

B. Wave energy and growth rate

The total energy of the wave consists of three components, the kinetic energy

$$E_k = \frac{1}{2} \rho \int_V \mathbf{u}_{\text{irrot}}^2 dV, \quad (14)$$

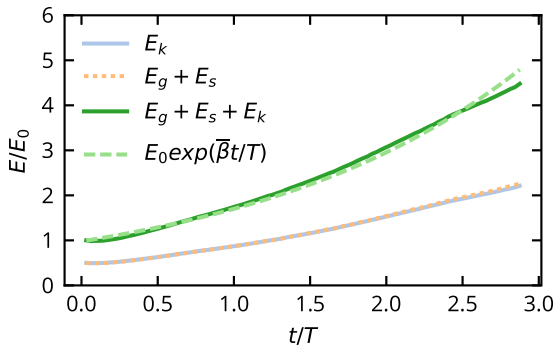


FIG. 3. Example of the wave energy extracted from the simulation output surface elevation $\eta(x, t)$, for $\text{Re} = 5513$, $\text{Bo} = 1.47$, and $u_*/c = 1$. Equal partition between the kinetic E_k and the potential energy $E_g + E_s$ is shown by the overlapping blue solid line and orange dotted line. The total wave energy (green solid line) is the sum of the kinetic and potential energy. The growth rate of the wave $\bar{\beta}$ is computed by fitting an exponential curve to the total energy budget (dashed line). All growing cases present a similar energy budget during the initial growth, where the wave remains of low amplitude.

the gravitational potential energy $E_g = \rho g \int_V y dV$, and surface energy $E_s = \sigma \int_S dA$. For 2D waves, we have

$$E_g = \frac{1}{2} \rho g \int \eta(x, t)^2 dx + \text{const}, \quad (15)$$

$$E_s = \sigma \int (\sqrt{1 + (\partial\eta/\partial x)^2} - 1) dx \quad (16)$$

where the constant is a gauge to have zero energy when the interface is flat. In the linear regime, E_s/E_g is proportional to the Bond number, and there should be equal partition between potential energy $E_g + E_s$ and kinetic energy E_k in the linear wave regime. The total wave energy is then given by

$$E(t) = E_k(t) + E_g(t) + E_s(t). \quad (17)$$

The surface tension E_s and gravity E_g energy terms are computed from the interface elevation $\eta(x, t)$, and the wave kinetic energy E_k is computed using the irrotational wave velocity field $\mathbf{u}_{\text{irrot}}$ obtained as described in Sec. III A. In Fig. 3, E_k , $E_g + E_s$ and E are plotted, and equal partition is clearly recovered between kinetic and potential energy terms. For simplicity, E_s and E_g are not plotted separately, but it is worth noticing that E_s has a nontrivial contribution to the total energy in all cases discussed here, in contrast to higher Bond number waves (typically $\text{Bo} > 20$) for which the surface tension energy becomes negligible [26].

The wave energy in Fig. 3 is growing exponentially and can be fitted by

$$E(t) = E_0 \exp(\beta t) = E_0 \exp(\bar{\beta} t/T), \quad (18)$$

where E_0 is the initial wave energy and $T = 2\pi/\omega$ is the wave period computed from the dispersion relation, so that the growth rate β is the only adjustable parameter determined by fitting the data. This yields the nondimensional growth rate $\bar{\beta} = (T/E)\partial E/\partial t$. All (growing) cases summarized in Table I present an initial growth regime similar to the one shown in Fig. 3, with equal partition between potential and kinetic energy and a growth that can be described as exponential as long as the wave amplitude remains small (typically a wave slope $ak < 0.1$). We systematically obtain the growth rate $\bar{\beta}$ as a function of the controlling parameters Re , Bo , and u_*/c .

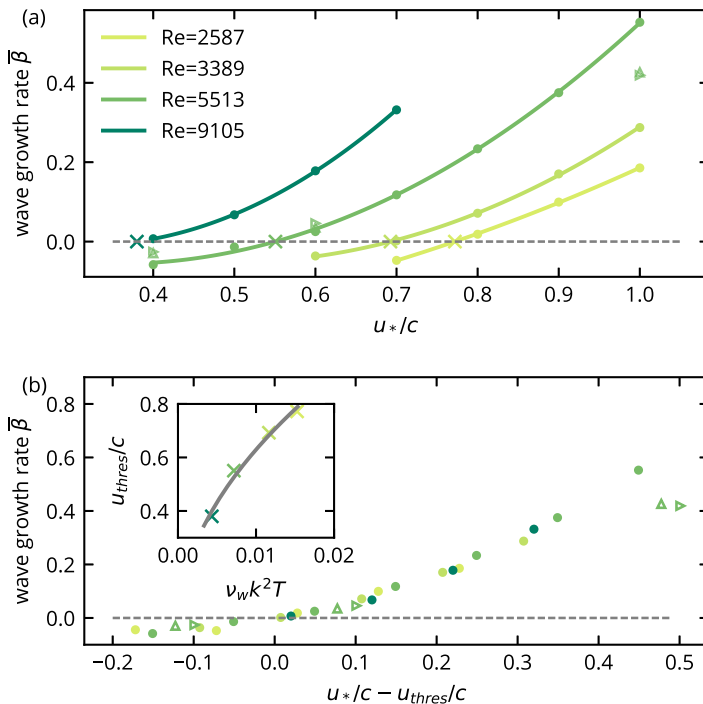


FIG. 4. (a) Nondimensional wave growth rate as a function of inverse wave age u_*/c for different nondimensional numbers (Re and Bo). The gray dotted line marks the cutoff between wave growth and decay due to viscous dissipation. Wave growth increases with increasing wind forcing u_*/c . The intersection of the fitted curve with the cutoff line gives the threshold value for wave growth, denoted by u_{thres}/c and plotted in the inset of (b). The nonmatching high Bond number cases are shown with triangles: Bo = 25, \triangle ; Bo = 200, \triangleright . There is a weak dependency on Bond number for growth rate at higher u_*/c and growth threshold u_{thres}/c . All the growth rates are computed from the early stage when the energy curve is approximately exponential with a constant growth rate, and the wave slope remains below 0.1. (b) Nondimensional wave growth rate as a function of wind forcing accounting for the threshold $(u_* - u_{\text{thres}})/c$. Data across different Re are collapsed onto a single curve. Inset shows the threshold values u_{thres}/c as a function of the normalized viscous timescale. The gray fitted curve is $u_{\text{thres}}/c = 6.76\sqrt{\nu_w k^2 T}$.

C. Wave growth rate and threshold

Figure 4(a) shows the nondimensional growth rate $\bar{\beta}$ as a function of inverse wave age u_*/c , for sets of different Re and Bo. Under a fixed Re, the growth rate increases with u_*/c , and is positive only above a certain threshold u_{thres}/c , marked by the intersections of the fitted curves with the $\bar{\beta} = 0$ line. These threshold values are decreasing when Re is increasing, as lighter wind is able to make less viscous waves grow. We comment that the normalized growth rate α [see Eq. (1) for its definition] is within the range of experimentally reported data compiled in [8]. The growth rate also shows a weak dependency on the Bond number.

The threshold can be understood by balancing the viscous dissipation rate of linear waves $4\nu_w k^2$ [36] and the growth rate due to the wind forcing,

$$\rho_w \nu_w k^2 \sim \rho_a (u_*/c)^2 / T, \quad (19)$$

which suggests that the threshold for growth scales as $u_{\text{thres}}/c \propto \sqrt{\nu_w k^2 T}$. The gray curve in the inset of Fig. 4 shows indeed this scaling relationship. The values are close in magnitude to the

wave onset threshold found in the experiment done with water in [28], although the experimental conditions are quite different from our numerical setup.

We find that the growth rates are better collapsed if plotted against the shifted variable $u_* - u_{\text{thres}}$ instead of u_* , as shown in Fig. 4(b). This indicates that the growth rate from wind input does not simply scale with $(u_*/c)^2$, and the viscous effect plays a more complicated role than that included by the $4\nu k^2$ damping term. Otherwise a $(u_*^2 - u_{\text{thres}}^2)/c^2$ scaling would be expected, which is not the case with the growth rates we collected in the present configuration. A theoretical explanation behind the variable $u_* - u_{\text{thres}}$ requires further investigation and appears to result from a combination of viscous and pressure stress forcing, instead of the pressure-dominated forcing scenario. Also, the pressure variation might originate from a different mechanism than the one described in Miles's classic work [3] given the linear laminar wind profile.

D. Subsurface drift development

At the same time the wave grows, a layer of subsurface shear current with velocity u_{drift} develops, visible in Fig. 2. This layer of vorticity is the viscous fluid's response to the strong wind shear stress present in our configuration (see Fig. 1) and should not be confused with the thin vorticity layer near the surface of freely propagating waves (see, e.g., [17,38]), which is much thinner and is characterized by a viscous boundary layer of order $\delta_{\text{wave}} \sim \lambda/\sqrt{\text{Re}}$ [26], as illustrated in Appendix B.

There are two features systematically characterizing the subsurface drift development under this linear wind shear: an increasing surface drift velocity and an increasing drift layer thickness as time advances. To describe it quantitatively, we consider the phase average $u_{\text{drift}}(x, y, t)$ over one wavelength, denoted $u_d(y, t)$. Admittedly the drift layer is not strictly uniform along the wave phase, but this 1D profile $u_d(y, t)$ is able to capture the major dynamics quite well and can be readily modeled as viscous momentum diffusion driven by a constant shear stress at the boundary. We follow the model proposed in [33] to describe the development of a viscous drift under wind forcing in a laboratory experiment, which ignores the presence of the initial wave and considers the following 1D diffusion equation over a flat boundary:

$$\partial_t u_d = \nu_w \partial_{yy} u_d, \quad (20)$$

where $\nu_w = \mu_w/\rho_w$ is the kinematic viscosity of water. The boundary conditions are (considering a flat interface at $y = 0$)

$$u_d(y, 0) = 0 \quad \text{for } t \leq 0, \quad (21)$$

$$u_d(y, t) \rightarrow 0 \quad \text{as } y \rightarrow -\infty, \quad (22)$$

$$\mu_w \partial_y u_d(y, t) = \tau \quad \text{at } y = 0. \quad (23)$$

This model follows the one developed in [33] that describes time dependency of the surface drift for more general cases where shear stress is a polynomial of time $\tau = \sum a_k t^k$. In our configuration, $\tau = \rho_a u_*^2$ and can be seen as a constant (to a good approximation). Solving this diffusion equation gives the time-dependent 1D profile

$$u_d(y, t) = \tau \Gamma(1) \frac{\sqrt{\nu_w t}}{\mu_w} \frac{2}{\sqrt{\pi}} \exp(-y^2/8\nu_w t) D_{-2}(\sqrt{y^2/8\nu_w t}), \quad (24)$$

where D_{-2} is the parabolic cylinder function. The profiles at different time are plotted in Fig. 5(a), which shows the intensification of the drift at the surface and the thickening of the layer with time for a particular configuration. Figure 5(b) shows the same profiles scaled by the similarity variable $\sqrt{\nu_w t}$. We can see that the boundary layer thickness scaling $\sqrt{\nu_w t}$ works well in collapsing all the curves, and there is an excellent agreement with the analytical solution Eq. (24) derived in [33]. It is an indication that the wave motion and drift velocity can actually be considered separately in this

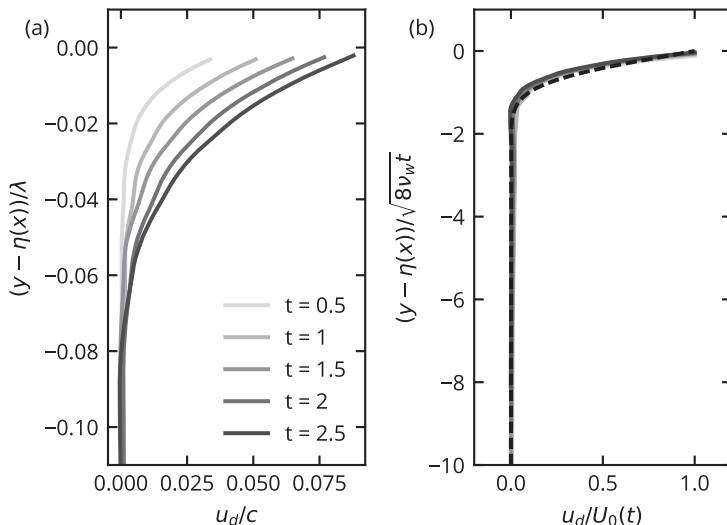


FIG. 5. (a) Vertical shear layer profile evolution with time. The profiles are phase averaged over the wavelength, for $\text{Re} = 5513$, $\text{Bo} = 1.47$, and $u_* / c = 0.8$, and time increases from light to dark lines. The evolution is similar across different parameter values. As time advances, the drift layer becomes thicker and more intense. (b) The same profiles with y scaled by the similarity solution variable $\sqrt{8\nu_w t}$ and u_d scaled by $U_0(t)$. All profiles collapse onto a single curve, which is in good agreement with the analytical solution from [33] [Eq. (24)].

linear regime. All simulations present a similar subsurface drift development as long as the wave amplitude remains small.

The evolution of surface drift velocity $U_0(t) = u_d(y = \eta(x, t), t)$ can be directly obtained by taking $y = 0$ in Eq. (24) and reads

$$U_0(t) = \tau \frac{\Gamma(1)}{\Gamma(3/2)} \frac{\sqrt{\nu_w t}}{\mu_w} = u_*^2 \frac{\rho_a}{\rho_w} \frac{\Gamma(1)}{\Gamma(3/2)} \sqrt{t/\nu_w}. \quad (25)$$

Figure 6 shows the normalized surface drift velocity $U_0(t)\sqrt{\nu_w/T}/u_*^2$ as a function of normalized time t/T for different Re (and corresponding Bo) and increasing values of the inverse wave age u_* / c .

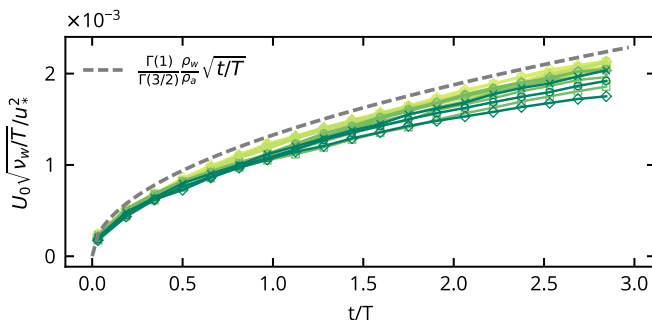


FIG. 6. Surface drift velocity $U_0(t)$, normalized according to the self-similar solution Eq. (25) as a function of time t/T . Color code is the same as in Fig. 4, corresponding to various Re , and markers show different inverse wave age u_* / c values: $u_* / c = 0.5$ (\times), 0.6 (\circ), 0.7 (\diamond), 0.8 (\triangle), 0.9 (\square). All data collapse onto a single curve for various u_* / c and Re , close to the analytical solution Eq. (25), shown with the dotted line.

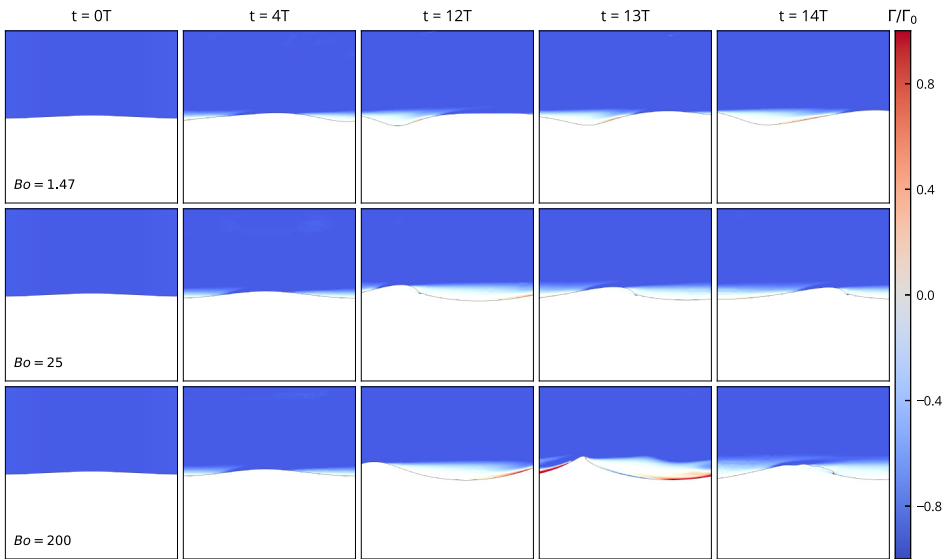


FIG. 7. Example of nonlinear development of the waves under the linear shear wind forcing. The wave shape evolution for $u_*/c = 1$, $\text{Re} = 5513$, and $\text{Bo} = 1.47, 25$, and 200 , is shown representing nonlinear capillary waves (top row), parasitic capillary waves (middle row), and spilling breakers (bottom row) respectively. (At $\text{Bo} = 1000$, we get a plunging breaker, which is not included here.) The color is air vorticity $\Gamma = \partial v/\partial x - \partial u/\partial y$ normalized by the initial velocity profile slope $\Gamma_0 = \rho_a u_*^2/\mu_a$. Air-flow separation is observed in all these nonlinear regimes, with the spilling breaking case showing the most significant feature.

The numerical time evolution of the drift surface velocity follows the analytical solution Eq. (25) quite well, and data across the parameter space all follow the similarity viscous scaling $(t/\nu_w)^{1/2}$, again as long as the wave amplitude remains small and the wave slope is below $ak < 0.1$.

IV. TOWARDS NONLINEAR WAVES

A. Wave shape and nonlinear regimes

In the previous sections, we discussed the growth of the drift layer and wave amplitude in the small amplitude limit, corresponding to wave slope below 0.1. We restricted the growth rate calculations using data before the wave amplitude has doubled (energy quadrupled). At this stage, there is no obvious separation of the airflow, and the change to the airflow velocity profile is also negligible. The growth threshold can be explained with a viscous scaling relation. When u_*/c is above the threshold, waves grow in an exponential manner, and the growth rate $\bar{\beta}$ is found to be a function of parameters u_*/c and Re , but not a strong function of the amplitude ak . The growth of the drift layer at this stage matches well with the analytical solution from the 1D viscous diffusion equation. As the simulation runs for longer times, and wind keeps inputting energy into the wave field, the wave amplitude further increases, and nonlinear features emerge. We present here a qualitative discussion of the nonlinear regimes that can be observed for various Bond numbers, which present similarities to regimes described in the literature through laboratory experiments (e.g., [39]) and numerical simulations (e.g., [17,18,26]).

In Fig. 7 we show three sequences of wave growth with increasing Bond number, ranging from a small value ($\text{Bo} = 1.47$) corresponding to mostly capillary waves, to an intermediate one ($\text{Bo} = 25$) where both gravity and capillarity are important and up to a higher value ($\text{Bo} = 200$) where gravity dominates. These simulations are performed at a fixed Reynolds number, $\text{Re} = 5513$. In other words, we are no longer matching Bo and Re as we did for the cases shown in Sec. III. The

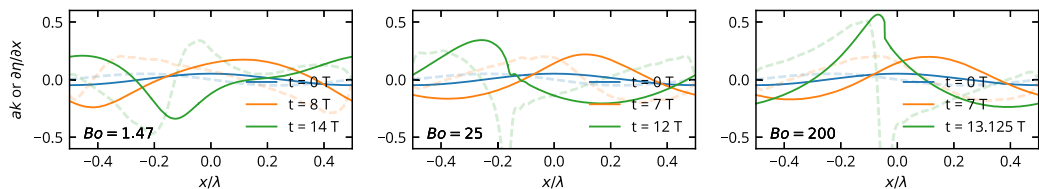


FIG. 8. Representative snapshots of wave shape (solid lines) and slope $\partial\eta/\partial x$ (dotted lines) for $Bo = 1.47, 25, 200$, $Re = 5513$, $u_*/c = 1$. This figure highlights the asymmetric wave shape for nonlinear waves at different Bond number. For $Bo = 1.47$, we observe nonlinear capillary waves; for $Bo = 25$, we observe parasitic capillary waves on the leeward; for $Bo = 200$, the wave first becomes short-crested and then it forms a spilling breaker.

$Bo = 25$ and 200 cases can be interpreted as water waves of wavelength 8.6 and 24.4 cm while being more viscous than real waves of the same wavelength. The color indicates the vorticity in the air, and it is clear that there is separation behind the crest for all cases when the amplitude is high enough. Initial wave growth for all cases is similar with the wave amplitude increasing and without significant change in wave shape; however, as the wave amplitude increases beyond the linear stage, there starts to be airflow separation, and the wave dynamics become different depending on the Bond number.

The first row shows the $Bo = 1.47$ configuration (with $Re = 5513$, corresponding to a wavelength of 2.1 cm) under the wind forcing during the later stages of the time evolution. We observe at later stages ($t/T = 12$ to 14) the development of a nonlinear capillary wave, while the increase in amplitude appears to slow down as the higher amplitudes are reached (due to the enhanced dissipation related to vorticity generation near curved interfaces). The nonlinear capillary wave displays a rounded crest and narrow trough, while a clear recirculation area in the air flow is visible, similar to airflow separation for gravity waves. The second row shows the $Bo = 25$ case and we observe that parasitic capillary waves start to develop on the forward face when the local slope $\eta_{\max}k \approx 0.4$, around $t/T = 12$. The train of capillaries propagates on the forward face of the wave, and there is associated vorticity generation underwater, together with airflow separation in the air phase. At some point, the wave amplitude starts to decrease, due to the enhanced dissipation induced by the parasitic capillary waves ($t/T = 14$). The third row shows the $Bo = 200$ case, and as the amplitude grows, the crest becomes sharper, and we observe a spilling breaker when the local slope becomes too high, $\eta_{\max}k \approx 0.57$ ($t/T = 13$), and the wave collapse on its forward face. Strong airflow separation is observed in this configuration, and wave energy loss is visible through the reduced amplitude that follows the collapse of the wave.

All these results are in general agreement with the different regimes reported in wind wave experiments [39] for parasitic capillary waves and spilling breakers, and in previous DNS work on capillary effect on wave breaking (without wind) [26,40], as well as in numerical work on waves forced by a pressure forcing term [17,18]. Note that the dynamics of spilling breakers in the laboratory (for mechanically forced waves), described in [41], are also similar to the regime observed here.

We highlight the asymmetric wave shapes at the nonlinear stage for these three cases by plotting η and $\partial\eta/\partial x$ for three representative times in Fig. 8. At $Bo = 1.47$, the nonlinear capillary wave shows a rounded crest and narrow trough, which is in agreement with the analytical solution derived in [42] for irrotational pure capillary waves. Due to the effect of the wind, the crest also shows asymmetry in the x direction, which is not the case for free traveling waves in [42]. When the nonlinear wave further develops, it seems that another crest of smaller wavelength starts to develop near the trough, which looks strikingly similar to the steady solution obtained under strong forcing conditions in [17]. At $Bo = 25$, the parasitic capillary waves forming on the leeward are very similar both to those described in the literature for similar parameters [26] without wind

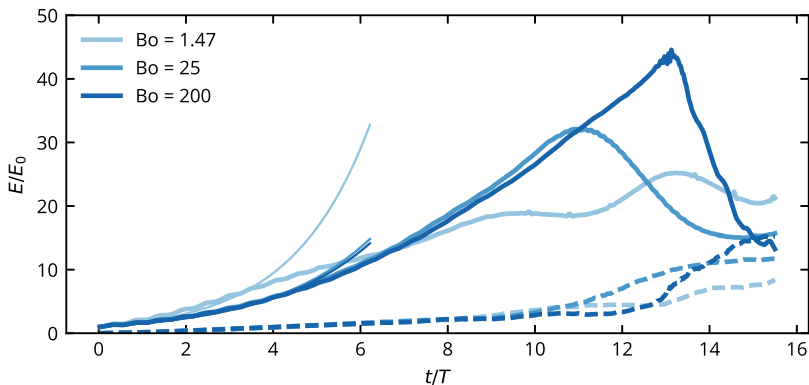


FIG. 9. The energy curve before and after breaking, for $Bo = 1.47, 25, 200$, $Re = 5513$, $u_* / c = 1$. The solid lines are the wave energy obtained by considering the kinetic and potential wave energy, following the velocity decomposition as described in Sec. III A. The dotted lines are the corresponding rotational kinetic energy. Note that this decomposition is not well defined in the nonlinear regime but provides an approximate partition. The thin solid line represent the exponential fit during the initial growth stage. For $Bo = 1.47$, oscillations in the wave energy correspond to the appearance of nonlinear capillary waves with high curvature, which induces a loss of energy (into rotational kinetic energy). For $Bo = 25$, parasitic capillary waves are formed around $t/T = 11$ and induce a significant loss in wave energy. Parasitic capillary waves form earlier than spilling breakers, but both induce a significant amount of wave energy transferred into drift.

but with finite amplitude Stokes wave initialization, and to earlier ones obtained using different numerical methods [17,43]. At $Bo = 200$, the wave first becomes short-crested, which is commonly observed for wind, and is found to happen when waves travel downstream the underlying current [34] (in our setup the current is the drift layer). A spilling breaker then forms, which has been observed experimentally in this wavelength range and discussed extensively in, e.g., [41]. The wave breaks at a higher slope than previously observed with simulations that initialize with a steep Stokes wave without wind forcing, which indicates that the process leading to breaking might have an effect on the breaking threshold. Again, this spilling breaker obtained with the linear wind shear forcing is very similar to the one obtained in [26] without wind forcing, starting from a high slope wave.

In general, the nonlinear wave shapes shown here are in good agreement with existing experimental and numerical studies. This is a remarkable point in itself since previous numerical works used different numerical methods and forcing conditions (a steady solution of potential flow with viscous boundary layer and pressure forcing in [17]; single-phase DNS with prescribed pressure and shear stress forcing in [43]; while other studies on spilling breakers and parasitic capillary waves did not consider any air-side forcing [26,40]). This, together with the general qualitative agreement with experimental studies [39,41], suggests that the nonlinear stage dynamics might not be strongly dependent on the specific forcing mechanism.

B. Energy budget in the nonlinear regime

Figure 9 shows the energy curves of the three cases discussed above: $Bo = 1.47, 25, 200$ at $Re = 5513$, and for $u_* / c = 1$. After the initial exponential growth stage, waves at different Bond number demonstrate very different time evolution scenarios, corresponding to the nonlinear dynamics described above: steep capillary wave, parasitic capillary waves, and spilling breaker. In all cases, the energy growth departs the exponential growths after four to five wave periods, corresponding approximately to the moment the wave slope becomes higher than 0.1.

For $Bo = 1.47$, as the nonlinear capillary waves grows in amplitude, the total wave energy keeps increasing at approximately a linear rate, before showing energy oscillations around

$t/T = 10$, when very steep capillary wave is observed (see Fig. 7). These oscillations are linked to the energy loss associated with vorticity generation when high-curvature regions appear.

For $Bo = 25$, the formation of parasitic capillary waves on the forward face of the wave at $t/T \approx 11$ leads to a wave energy loss and corresponds to energy transfer from the wave into the rotational kinetic energy or subsurface drift and introduces a large amount of dissipation, the wave losing about half of its total energy within two wave periods. This transfer results from the high-vorticity region induced by the large curvature of the parasitic capillary waves [38] and is independent of the wind forcing. The wave amplitude decreases because of the transfer of energy and increased dissipation. It is important to notice that this description of parasitic capillary waves and their role in energy dissipation is in close agreement with previous studies [17,26,29,40], with and without wind forcing, suggesting that the process is independent of the details of the air flow.

For $Bo = 200$, a spilling breaker happens at $t/T \approx 13$, once the wave has reached a relatively high slope, later than the parasitic capillary wave. This breaking process is associated with a dramatic drop in the wave energy and a significant increase in the rotational kinetic energy (subsurface drift) energy. Again, the magnitude of the energy loss due to breaking during the spilling process is very similar in magnitude to that found in a previous study [26], which indicates that once breaking is triggered, the decay rate is independent of the wind forcing and is insensitive to the viscosity at high enough Re .

V. CONCLUSION

We investigated the wind wave growth problem of gravity-capillary waves in the viscous regime, with direct numerical simulations that solve the two-phase Navier-Stokes equations using an adaptive mesh refinement and VoF interface reconstruction, under a simplified 2D laminar setup. The results show that the wave growth and the drift development can be analyzed in a relatively independent manner in the linear stage. The wave growth rates across a parameter space of Bo , Re , and u_*/c are reported. The growth/decay threshold computed from numerical experiments can be explained by balancing the viscous damping and wind input rate. The wave growth rate in the viscous regime can be better described by using a $u_*/c - u_{\text{thres}}/c$ variable that includes the viscous effect, although the specific functional form of the growth rate remains to be fully understood. The drift development can be described by a diffusion equation, which leads to the similarity solution for the surface drift velocity and vertical profile. In the early stage when the amplitude is small, most of the momentum is transferred into the drift. For the cases where u_*/c is below the growing threshold, the dynamics more closely resemble a wind-driven water boundary layer. The nonlinear growth stage is also discussed. We recover various wave shapes and dynamics as a function of the Bond number, including steep nonlinear capillary waves, parasitic capillary waves, and spilling breaking. We observe energy transfer from the wave field to the subsurface current when parasitic capillary waves are formed or when wave breaking occurs.

In summary, this numerical setup permits study of the full life cycle of short waves, from exponential growth of small amplitude waves, to nonlinear wave growth leading to breaking. We observe an associated development of a drift layer beneath the wave, as well as air flow separation above the steep waves, and modification of the initially linear shear profile in the air. However, we should keep in mind that the present setup is 2D and laminar, hence the specific forcing mechanism and later stage separation patterns with a turbulent boundary layer will likely be different. The full cycle simulation has provided us with a valuable physical picture of wind wave growth, and future work should focus on providing a more accurate representation of the 3D turbulent wind structure. This has long been a challenging task for numerical works on wind wave interaction, and it is the plan of future work to extend the current setup to 3D simulations with the coupled air-water turbulent boundary layers, which will allow a more complete study of pressure and shear stress forcing and wave-wind-current interactions.

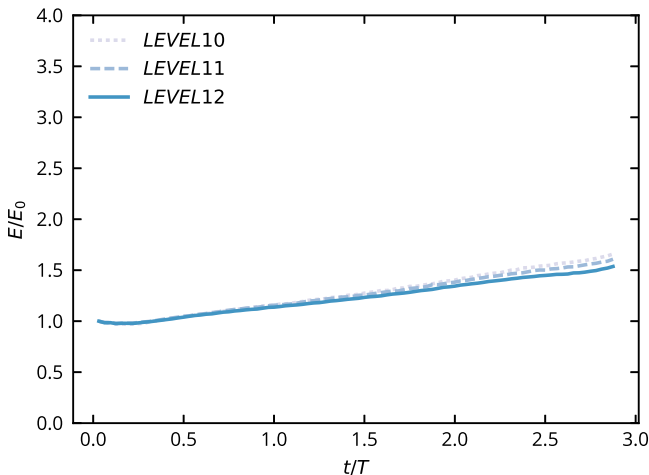


FIG. 10. Total energy budget for the case $Re = 9105$, $Bo = 3.31$, and $u_*/c = 0.6$, showing the convergence of the results with respect to grid size. The results are very similar between the maximum refinement levels 10, 11, and 12. Level 9 causes development of 2D vortex instabilities and is not considered.

ACKNOWLEDGMENTS

This work has been supported by NSF Grant 1849762 (Physical Oceanography). We thank the anonymous reviewers for their helpful comments, which have helped improve the manuscript.

APPENDIX A: NUMERICAL CONVERGENCE

Here we give a brief verification of grid convergence. Considering a length L_0 domain and a maximum refinement level N adaptive mesh, the effective resolution is $\Delta x = L_0/2^N$. Plotted in Fig. 10 are the total energy curves obtained under three refinement levels for the highest Re case (which requires the finest grids to resolve). Between levels 10, 11, and 12 there is satisfactory grid convergence, and the results shown above are all of level 11. All cases present similar convergence curves. Going below level 10, it exhibits instability in the air shear flow and the energy curve does not have physical meaning and is not plotted here.

For grid resolution in terms of wall unit, although the airflow is not turbulent, we *can* still define wall unit in a similar manner, i.e., $\delta_v = \nu_a/u_*$, and in the most demanding case (with $Re = 20\,000$, $u_*/c = 0.7$), we have an effective resolution about 0.2 wall unit, i.e., $\Delta(y^+) = 0.2$. $\Delta(x^+)$ is the same as $\Delta(y^+)$ because adaptive mesh refinement does not differentiate between the x and y directions.

APPENDIX B: ON THE VORTICITY IN A VISCOUS FLUID

In this section, we clarify that the source of the vorticity in water (what we call drift layer) is mainly from wind shear stress, by giving a visualization of vorticity in the water without and with wind forcing in Fig. 11.

It has been theoretically established [38] that in free propagating surface waves, even though the interior of the water can be approximated as irrotational, as long as the fluid is viscous, there is a thin layer of viscosity near the surface. This is because the boundary condition of zero stress (free surface) must be satisfied. More specifically, to the first order in ak ,

$$\Omega_w = \Omega_0 e^{\alpha n},$$

where $\Omega_0 \equiv 2(\partial v/\partial y)_{y=0}$, and $\alpha = (-i\omega/\nu_w)^{1/2}$ [see Eq. (3.6) in [38]]. Here Ω_w is used to denote the vorticity in the water while ω is the wave frequency, the same as in Fig. 11. n is the outward

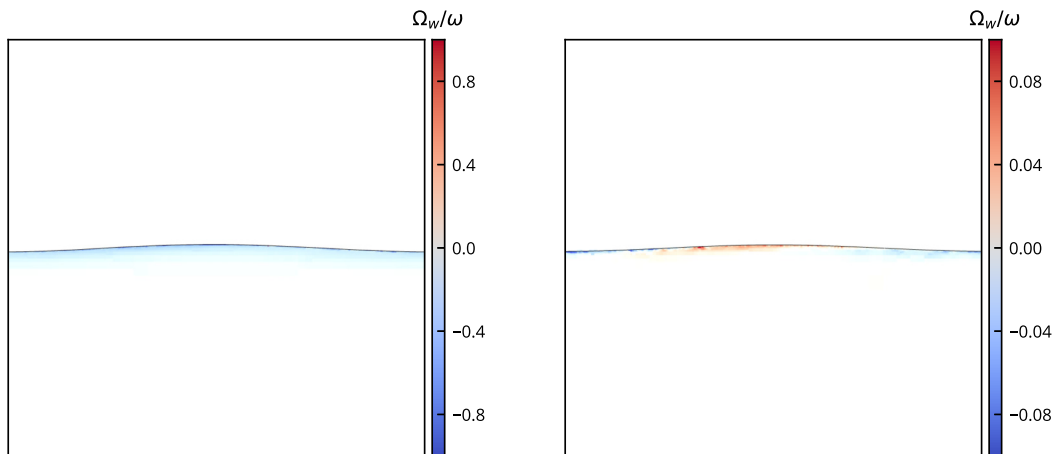


FIG. 11. Vorticity in water Ω_w normalized by wave frequency ω , for propagating waves at $\text{Re} = 3389$ and $\text{Bo} = 0.53$. Here $t = 2T$, and the initial wave slope $ak = 0.05$. Left: No wind, a thin vorticity layer is visible with alternating sign, and its thickness δ_1 does not increase with time. This corresponds to the free surface vorticity described in [38]. Right: There is wind and $u_*/c = 0.8$. The vorticity layer is much more intense and thickness δ_2 develops over time. Note the order of magnitude difference in the color scale.

normal, and $(\partial v/\partial y)_{y=0}$ is the vertical velocity gradient at the surface. This means that the vorticity induced by this mechanism is of alternating sign and does not penetrate a distance of order $\delta_1 = (v_w/\omega)^{1/2}$. This is verified by running a case with the same wave initialization, but without wind, shown on the left in Fig. 11. To the second order in ak , it is derived in [38] that there is a mean vorticity $\Omega_w = -2(ak)^2\omega$ beyond the thin boundary layer $\delta_1 = (v_w/\omega)^{1/2}$ but this effect is neglected in this initial stage.

In our simulation setup, with shear stress forcing, the vorticity layer is almost uniform and much more intense. Its dynamics are described in Sec. III D, and the thickness δ_2 scales with \sqrt{vt} .

Figure 11 shows the vorticity in a pair of no wind and $u_*/c = 0.8$ cases; it is clear that the vorticity in the latter is an order of magnitude higher than in the former. Therefore, we conclude the decomposition proposed in Sec. III A is reasonable as the shear induced drift is dominant in all cases. However, an unambiguous decomposition of the velocity field into wave and drift for the nonlinear stage is nontrivial, and the discussion in Sec. IV is mostly qualitative.

-
- [1] P. P. Sullivan and J. C. McWilliams, Dynamics of winds and currents coupled to surface waves, *Annu. Rev. Fluid Mech.* **42**, 19 (2010).
 - [2] P. Janssen, *The Interaction of Ocean Waves and Wind* (Cambridge University Press, Cambridge, 2004).
 - [3] J. W. Miles, On the generation of surface waves by shear flows, *J. Fluid Mech.* **3**, 185 (1957).
 - [4] O. M. Phillips, On the generation of waves by turbulent wind, *J. Fluid Mech.* **2**, 417 (1957).
 - [5] G. R. Valenzuela, The growth of gravity-capillary waves in a coupled shear flow, *J. Fluid Mech.* **76**, 229 (1976).
 - [6] A. Zeisel, M. Stiassnie, and Y. Agnon, Viscous effects on wave generation by strong winds, *J. Fluid Mech.* **597**, 343 (2008).
 - [7] W. J. Plant, A relationship between wind stress and wave slope, *J. Geophys. Res.* **87**, 1961 (1982).
 - [8] W. L. Peirson and A. W. Garcia, On the wind-induced growth of slow water waves of finite steepness, *J. Fluid Mech.* **608**, 243 (2008).

- [9] M. P. Buckley, F. Veron, and K. Yousefi, Surface viscous stress over wind-driven waves with intermittent airflow separation, *J. Fluid Mech.* **905**, A31 (2020).
- [10] K. Yousefi, F. Veron, and M. P. Buckley, Momentum flux measurements in the airflow over wind-generated surface waves, *J. Fluid Mech.* **895**, A15 (2020).
- [11] D. Yang and L. Shen, Direct-simulation-based study of turbulent flow over various waving boundaries, *J. Fluid Mech.* **650**, 131 (2010).
- [12] L. Grare, W. L. Peirson, H. Branger, J. W. Walker, J.-P. Giovanangeli, and V. Makin, Growth and dissipation of wind-forced, deep-water waves, *J. Fluid Mech.* **722**, 5 (2013).
- [13] P. P. Sullivan, J. C. McWilliams, and C.-H. Moeng, Simulation of turbulent flow over idealized water waves, *J. Fluid Mech.* **404**, 47 (2000).
- [14] P. P. Sullivan, J. C. McWilliams, and E. G. Patton, Large-eddy simulation of marine atmospheric boundary layers above a spectrum of moving waves, *J. Atmos. Sci.* **71**, 4001 (2014).
- [15] N. T. Husain, T. Hara, M. P. Buckley, K. Yousefi, F. Veron, and P. P. Sullivan, Boundary layer turbulence over surface waves in a strongly forced condition: LES and observation, *J. Phys. Oceanogr.* **49**, 1997 (2019).
- [16] D. Yang, C. Meneveau, and L. Shen, Dynamic modelling of sea-surface roughness for large-eddy simulation of wind over ocean wavefield, *J. Fluid Mech.* **726**, 62 (2013).
- [17] A. V. Fedorov and W. K. Melville, Nonlinear gravity–capillary waves with forcing and dissipation, *J. Fluid Mech.* **354**, 1 (1998).
- [18] W.-T. Tsai, S.-M. Chen, G.-H. Lu, and C. S. Garbe, Characteristics of interfacial signatures on a wind-driven gravity-capillary wave, *J. Geophys. Res. Oceans* **118**, 1715 (2013).
- [19] M.-Y. Lin, C.-H. Moeng, W.-T. Tsai, P. P. Sullivan, and S. E. Belcher, Direct numerical simulation of wind-wave generation processes, *J. Fluid Mech.* **616**, 1 (2008).
- [20] D. Yang and L. Shen, Simulation of viscous flows with undulatory boundaries: Part II. Coupling with other solvers for two-fluid computations, *J. Comput. Phys.* **230**, 5510 (2011).
- [21] S. Popinet, Gerris: A tree-based adaptive solver for the incompressible Euler equations in complex geometries, *J. Comput. Phys.* **190**, 572 (2003).
- [22] S. Popinet, An accurate adaptive solver for surface-tension-driven interfacial flows, *J. Comput. Phys.* **228**, 5838 (2009).
- [23] W. Mostert and L. Deike, Inertial energy dissipation in shallow-water breaking waves, *J. Fluid Mech.* **890**, A12 (2020).
- [24] J. A. van Hooft, S. Popinet, C. C. van Heerwaarden, S. J. A. van der Linden, S. R. de Roode, and B. J. H. van de Wiel, Towards adaptive grids for atmospheric boundary-layer simulations, *Boundary-Layer Meteorol.* **167**, 421 (2018).
- [25] A. Bagué, D. Fuster, S. Popinet, R. Scardovelli, and S. Zaleski, Instability growth rate of two-phase mixing layers from a linear eigenvalue problem and an initial-value problem, *Phys. Fluids* **22**, 092104 (2010).
- [26] L. Deike, S. Popinet, and W. K. Melville, Capillary effects on wave breaking, *J. Fluid Mech.* **769**, 541 (2015).
- [27] L. Deike, W. K. Melville, and S. Popinet, Air entrainment and bubble statistics in breaking waves, *J. Fluid Mech.* **801**, 91 (2016).
- [28] A. Paquier, F. Moisy, and M. Rabaud, Viscosity effects in wind wave generation, *Phys. Rev. Fluids* **1**, 083901 (2016).
- [29] W. K. Melville and A. V. Fedorov, The equilibrium dynamics and statistics of gravity–capillary waves, *J. Fluid Mech.* **767**, 449 (2015).
- [30] S. Perrard, A. Lozano-Durán, M. Rabaud, M. Benzaquen, and F. Moisy, Turbulent windprint on a liquid surface, *J. Fluid Mech.* **873**, 1020 (2019).
- [31] J. Wu, Laboratory studies of wind–wave interactions, *J. Fluid Mech.* **34**, 91 (1968).
- [32] W. K. Melville, R. Shear, and F. Veron, Laboratory measurements of the generation and evolution of Langmuir circulations, *J. Fluid Mech.* **364**, 31 (1998).
- [33] F. Veron and W. K. Melville, Experiments on the stability and transition of wind-driven water surfaces, *J. Fluid Mech.* **446**, 25 (2001).

- [34] A. F. Teles Da Silva and D. H. Peregrine, Steep, steady surface waves on water of finite depth with constant vorticity, *J. Fluid Mech.* **195**, 281 (1988).
- [35] X. Hu and T. Cubaud, Viscous Wave Breaking and Ligament Formation in Microfluidic Systems, *Phys. Rev. Lett.* **121**, 044502 (2018).
- [36] M. J. Lighthill, *Waves in Fluids* (Cambridge University Press, 2001).
- [37] H. Lamb, *Hydrodynamics* (Cambridge University Press, 1993).
- [38] M. S. Longuet-Higgins, Capillary rollers and bores, *J. Fluid Mech.* **240**, 659 (1992).
- [39] G. Caulliez, Dissipation regimes for short wind waves, *J. Geophys. Res. Oceans* **118**, 672 (2013).
- [40] W.-T. Tsai and L.-P. Hung, Enhanced energy dissipation by parasitic capillaries on short gravity–capillary waves, *J. Phys. Oceanogr.* **40**, 2435 (2010).
- [41] J. H. Duncan, Spilling breakers, *Annu. Rev. Fluid Mech.* **33**, 519 (2001).
- [42] G. D. Crapper, An exact solution for progressive capillary waves of arbitrary amplitude, *J. Fluid Mech.* **2**, 532 (1957).
- [43] W.-T. Tsai and L.-P. Hung, Three-dimensional modeling of small-scale processes in the upper boundary layer bounded by a dynamic ocean surface, *J. Geophys. Res.* **112**, C02019 (2007).